OAM driven nucleation of sub-50 nm compact antiferromagnetic skyrmions

Sougata Mallick, Peng Ye, Willem Boutu, David Gauthier, Hamed Merdji, Manuel Bibes, Michel Viret, Karim Bouzehouane, Vincent Cros

OAM driven nucleation of sub-50 nm compact antiferromagnetic skyrmions

Sougata Mallick[1,2*] | Peng Ye[3,4*] | Willem Boutu[3] | David Gauthier[3] | Hamed Merdji[5] | Manuel Bibes[1] | Michel Viret[6] | Karim Bouzehouane[1] | Vincent Cros[1]

[1]Laboratoire Albert Fert, CNRS, Thales, Université Paris-Saclay, 91767 Palaiseau, France

[2]Department of Physics and Nanotechnology, SRM Institute of Science and Technology, Kattankulathur- 603203, Tamilnadu, India

[3]Université Paris-Saclay, CEA, LIDYL, 91191 Gif sur Yvette, France, CY Cergy Paris Université, CEA, LIDYL, 91191 Gif sur Yvette, France

[4]Beijing National Laboratory for Condensed Matter Physics, Institute of Physics, Chinese Academy of Sciences, Beijing, China

[5]LOA, CNRS, Ecole Polytechnique, ENSTA Paris, Institut Polytechnique de Paris, Palaiseau, France

[6]SPEC, CEA, CNRS, Université Paris-Saclay, Gif sur Yvette, France

Correspondence
Sougata Mallick, and Vincent Cros
Email: sougata.physics@gmail.com, vincent.cros@cnrs-thales.fr

Funding information
EU Horizon 2020 research and innovation programme under the Grant No. 964931 (TSAR), CEFIPRA, and PEPR SPIN ANR-22-EXSP 0002 (CHIREX).

Owing to their high mobility and immunity to topological deflection, skyrmions in antiferromagnetic (AFM) systems are gaining attention as a potential solution for next generation magnetic data storage. Synthetic antiferromagnets (SAFs) offer a promising avenue to tune the properties of the individual magnetic layers, facilitating the conditions necessary for skyrmions to be used in practical devices. Despite recent advancements achieving fast skyrmion mobility, the nucleation of small and rigid circular skyrmions without an external field remains challenging in SAFs. Theoretical predictions suggest that optical vortex (OAM) beams can stabilize skyrmionic spin textures by transferring their spin and orbital angular momentum to the magnetic material. Here, we delve into this intriguing proposal and successfully demonstrate the creation of sub-50 nm compact skyrmions in SAFs using OAM beams, eliminating the need for external magnetic fields. Additionally, the results underscore the importance of beam energy and the number of pulses, as both factors play critical roles in the stabilization of these AFM skyrmionic textures. This breakthrough is significant as it paves the way for stabilizing true zero-field skyrmions in AFM systems, where magnetization is minimally affected by external magnetic fields. This work will open a potential avenue for stabilizing small, compact skyrmions in antiferroic systems, facilitating their implementation in logic and memory devices.

*Equally contributing authors.

1 | INTRODUCTION

Potential technological applications based on conventional ferromagnetic (FM) skyrmions face several inherent challenges [1], including the transverse deflection [2, 3] of skyrmions due to their non-zero topology and hence the risk of annihilation at device edges [2, 4], and the comparatively high power consumption [5] required to move them using spin-polarized currents, etc. Furthermore, in FM multilayers, the influence of interlayer dipolar fields results in the formation of larger skyrmionic bubbles instead of compact, nanometric skyrmions [6]. Additionally, in FM skyrmions, the displacement speed is limited due to dissipation [7, 8]. These challenges can be effectively mitigated by working with antiferromagnetic (AFM) skyrmions, which have the potential to operate at speeds significantly larger than their FM counterparts [9, 10, 11, 12]. The increased velocity in AFM solitons is a consequence of their intrinsic dynamics, dominated by the strength of the exchange energy [13]. Another key advantage of skyrmions in AFM systems is the significant reduction or even elimination of the skyrmion Hall effect [11, 14]. However, controlling and detecting non-collinear AFM order in perfectly compensated antiferromagnets can be difficult. To overcome this challenge, synthetic antiferromagnets (SAFs) offer an alternative solution [12, 15, 16]. SAFs are constructed using ultrathin FM layers that are antiferromagnetically coupled by a non-magnetic spacer layer through interlayer electronic coupling of the Ruderman–Kittel–Kasuya–Yoshida (RKKY) type [17]. In this context, metallic multilayers serve as an ideal platform for creating SAFs, where the strength of the RKKY coupling and interfacial Dzyaloshinskii-Moriya interaction (iDMI) can be finely tuned through the judicious selection of metallic interfaces on either side of the FM layers. However, it should be noted that, due to the compensation of the magnetization, SAFs remain nearly unaffected by magnetic fields smaller than the RKKY coupling. In this context, several novel methods have been employed to stabilize skyrmions in the absence of an external magnetic field, including the utilization of frustrated exchange interactions [18], the exchange bias effect [19], geometrical confinement [20, 21], etc. A more recent approach to stabilize skyrmions at remanence involves a combination of enhanced anisotropy along with a tailored magnetic field history, achieved through a series of minor loops [12, 22, 23]. However, skyrmions stabilized using the aforementioned strategies often exhibit a lack of rigidity, significantly larger size, and undergo run-out instability when subjected to electrical manipulation, primarily due to the orientation of the spin-orbit torques [12, 22, 24, 25]. A successful approach to stabilize compact (< 30 nm) AFM skyrmions in the absence of any external field involves the use of a bias magnetic field below the SAF heterostructure [16]. Here a bias layer with uniform magnetization ($\mathbf{m} = \mathbf{z}$) is required to couple ferromagnetically with one of the magnetic layers in order to promote the spin spirals along $\mathbf{z}$ and expand at the expense of the parts with $\mathbf{m} = -\mathbf{z}$. However, the incorporation of such a bias layer has proven to impede the effective optimization of spin torques necessary to propel skyrmions in SAFs. Moreover, in biased SAF configurations, the passage of current through the tracks often triggers domain formation or magnetization switching within the bias layer, consequently destabilizing the skyrmions. Due to these complexities, none of the reports so far could successfully demonstrate the solitonic properties of compact AFM skyrmions in SAFs.

This panorama underscores the necessity of exploring alternative methodologies to stabilize small DMI skyrmions [6] within SAFs without reliance on external magnetic fields or bias layers. Within this framework, optical vortex beams emerge as a promising solution. By imparting their orbital angular momentum (OAM) into magnetic materials, these beams have the potential to stabilize skyrmionic textures effectively [26, 27, 28, 29]. The connection between photon magnetic fields and local magnetic moments is facilitated through a coherent Zeeman or magneto-electric interaction, potentially benefiting from induced local temperature gradients [26, 27]. By precisely focusing the beam spot onto targeted regions of a film, one can imprint skyrmions in a controlled fashion. The larger size of the beam spot initially leads to the creation of a sizable skyrmion, which subsequently undergoes size reduction to accommodate the various interactions at play. In the present study, we introduce the first proof-of-concept for the nucleation and

stabilization of compact (<50 nm) skyrmionic spin textures in unbiased SAFs at remanence by employing OAM laser pulses. Furthermore, we underscore the significance of finely tuning the energy and number of pulses to enhance the role of the OAM effect while concurrently minimizing the impact of thermal energy.

2 | EXPERIMENTAL DETAILS

2.1 | Deposition of synthetic antiferromagnetic multilayer:

The SAF thin films have been grown at room temperature in a high-vacuum sputtering chamber with a base pressure of 5×10^{-8} mbar on thermally oxidized Si substrates. The sputtering offers an industry compatible process with excellent repeatability with a precision of individual layer thicknesses down to 0.03 nm. The multilayered samples have the following structure (starting from substrate side): Ta(10 nm)|Pt(8 nm)|Co(1.28 nm)|Ru(0.75 nm)|Pt(0.6 nm)|Co(1.28 nm)|Ru(0.75 nm)|Pt(3 nm). The bottom Pt layer helps to stabilize perpendicular magnetic anisotropy (PMA) and introduce DMI in the system whereas the top Pt serves as a capping layer. The RKKY AFM interlayer coupling is established through the combination of thin Ru|Pt layers. A detailed description of various energy and micromagnetic parameters in similar sample structure has already been reported in Legrand et al. [16]. It should be noted that the spin-reorientation transition (SRT) thickness for Co in the single layer film is ~ 1.5 nm. The Co layers in the SAF samples have been intentionally chosen a bit lower (1.28 nm) than the SRT thickness to provide higher magnetic anisotropy and thus facilitate hosting skyrmions at remanence [22].

2.2 | Generation of OAM beam:

The laser pulses used for this experiment are coming from a Starzz Optical Parametric Chirped Pulse Amplifier (OPCPA) from Amplitude, with a central wavelength of 1.8 µm and pulse duration of 40 fs (measured by the Frequency Resolved Optical Gating technique). The repetition rate of the laser can be externally controlled from single shot to 100 kHz. A combination of a half wave plate (HWP) and polarizer is used to control the pulse energy. The linear polarization of the laser is then switched to circular by a quarter wave plate (QWP), necessary to introduce an OAM (+1, 0, -1) in the beam by a Q plate (Arcoptix). A second QWP is used after the Q plate to control the polarization state of the final beam, allowing switching from linear to right or left circular. Finally, a telescope enlarges the beam in order to produce a smaller focus size on the sample after focusing. The intensity and phase distribution of a simulated Laguerre-Gaussian beam with an OAM=+1, are presented in Fig.1(a) and (b). The experimental spot size of the optimized OAM beam is $\sim$14 μm (Fig.1(c)). The nature of an OAM beam is understood from the distribution of the intensity (Fig.1(d)) along two directional cuts in (c) (the horizontal scale relates to the size on the detector, where the beam is enlarged by a microscope objective). The phase varies ortho-radially from 0 to 2π, however the phase gradient in the ortho-radial direction is very large at the center of the beam, where the intensity is minimum.

2.3 | MFM observation:

The magnetic force microscopy (MFM) observations of the SAF textures have been conducted under vacuum conditions (5×10^{-7} mbar). Room temperature images have been acquired using magnetic tips in a double-pass tapping-lift mode, with a lift height of 0 nm (however with different excitation amplitude). This mode involved detecting the phase shift during the second pass after a topographic measurement, enabling the probing of magnetic field gradients along the vertical direction. The raw AFM probes used are commercially available ultra-short cantilevers with a resonant

frequency of 300 kHz and a force constant of 0.3 N m^{-1}. These probes facilitates high-speed measurements in a high-vacuum environment, offering an excellent signal-to-noise ratio (with $Q > 500$). To fabricate the MFM tips, a bilayer coating of CoFeB (5 to 15 nm) and Al (5 to 30 nm) has been deposited in a sputtering chamber. The thickness of the bilayer coating has been carefully chosen to minimize the influence of stray fields originating from the tips on the magnetic textures within the samples, especially during the topographic measurement. A perpendicular magnetic field has been applied with a maximum uniform field of $\sim \pm 120$ mT. The apparent size of the skyrmions is determined by extracting the full width at half maximum (FWHM) from line scans of the textures. It should be noted that the apparent size of skyrmions observed via MFM is usually overestimated compared to their actual size, owing to the fact that the stray field is measured several tens of nm above the magnetic textures [16].

3 | RESULTS AND DISCUSSION

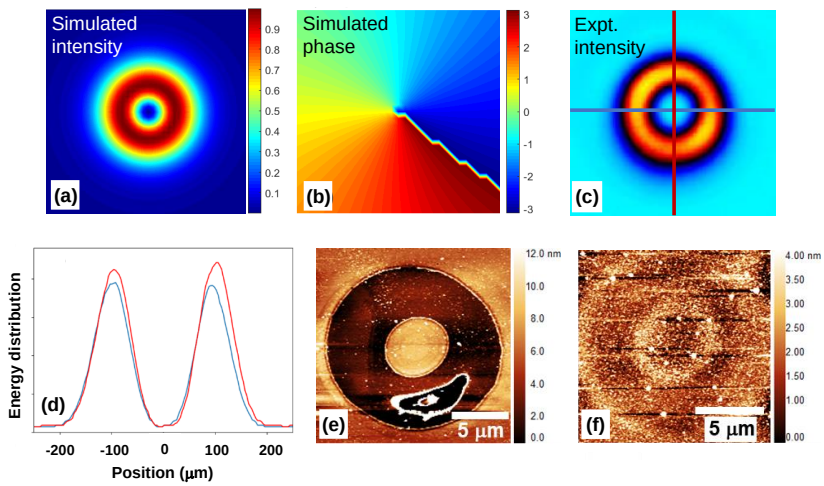

FIGURE 1 OAM beam characterization: (a) Simulated intensity profile of an OAM laser beam. (b) Simulated phase of a Laguerre-Gaussian beam carrying an OAM = +1. (c) Shape of an OAM beam with an experimental spot size of $\sim 14\,\mu$m. (d) The blue and red curves correspond to the vertical and horizontal cross-sections of the beam, respectively, as shown in (c). (e) and (f) topography of the thin films imaged with AFM after exposure to single-shot OAM beam with energy of ~ 810 nJ, and ~ 320 nJ, respectively.

The intensity profile of the experimental spot-size ($\sim 14\,\mu$m) of an OAM beam is shown in Fig.1(c). A noticeable feature in the beam spot is the concentration of energy predominantly within the ring-shaped region, indicated by the orange-red color. In contrast, the central portion of the beam, represented by the cyan circular area, exhibits the lowest intensity. Depending on its energy, the OAM beam affects the topography as demonstrated in Fig.1(e) and (f). In Fig.1(e), we show the impact of a single laser pulse OAM beam with large energy (~ 810 nJ). The region of the film corresponding to the ring area, which contains the majority of the pulse energy, experiences ablation that extends down to the bottom Pt layer, as confirmed by a topography scan revealing a depth of ~ 10 nm. It is worth emphasizing that despite the substantial beam intensity, the central portion of the beam spot remains unaffected from a topographical perspective. In another experiment, depicted in Fig. 1(f), the beam's energy has been chosen

to be significantly lower, ~ 320 nJ, resulting in a minimal topographical perturbation of less than 1 nm. To observe a significant impact from the OAM phase, fine-tuning at the center of the beam is necessary, as the pulse intensity (thermal contribution) is minimal at this point. Therefore, it is important to find a balance when selecting the energy of the beam, ensuring sizeable contribution from the OAM phase at the center while safeguarding the integrity of the rest of the sample from destruction.

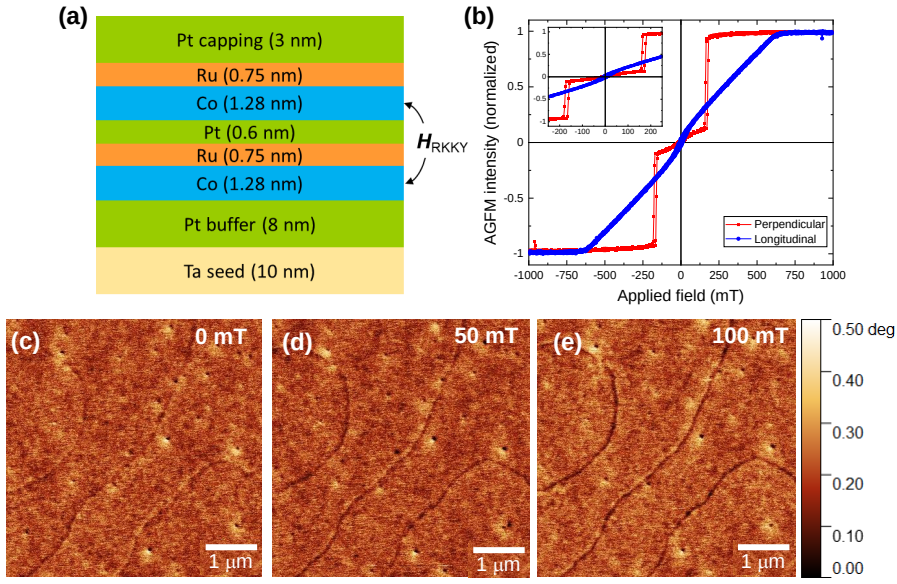

FIGURE 2 **SAF multilayer characterization:** (a) Cross-section of the schematic of the SAF multilayers showing the antiferromagnetic RKKY coupling between the two Co layers. (b) Hysteresis of the sample shown in (a) measured using an alternating gradient field magnetometer (AGFM) in both perpendicular and longitudinal configurations. Zoomed-in loops with AFM exchange field of ~ 170 mT is presented in the inset. (c)-(e) SAF DWs in the non-shot unperturbed area in the thin film at different external fields measured using vacuum MFM. The dark spots in the MFM images are appearing from the topography signal due to small lift height used for the measurements.

A schematic cross-section view of the SAF multilayer sample used in this work is presented in Fig.2(a). In Fig.2(b), we display the hysteresis curves as a function of the external magnetic field along perpendicular (red) and planar (blue) directions of the SAF multilayer sample. When the perpendicular field strength surpasses the AFM RKKY coupling threshold ($\mu_0 H_{RKKY}$) applied on both sides, the multilayer magnetization undergoes a reversal until it reaches saturation. The perpendicular hysteresis loop vividly demonstrates the robust PMA inherent in each FM layer within the SAF. This deliberate selection of sizable PMA is achieved through meticulous adjustment of the individual FM layer thicknesses to ensure the stability of skyrmions at remanence. The strength of the AFM coupling in this sample is $\mu_0 H_{RKKY} \approx$ 170 mT. In this study, we have chosen an experimental range of external perpendicular fields $\leq$ 100 mT (in absolute value) to avoid saturating the SAF. In Fig.2(c), we display an MFM image obtained in an area of the SAF multilayers that was not exposed to any laser pulse. Only two domains, separated by lines are present in the $5 \times 5\,\mu m^2$ image. The domains, as expected, have uniform antiferromagnetic configurations and hence do not generate any stray field leading to MFM contrast. However, the domain walls (DWs) appear as curved lines in the image. Additionally, we show the field dependence of such AFM DWs within our experimental range of external field in Fig.2(c)-(e). It is

observed that there is an incremental modification in the MFM phase intensity from 0.2° to 0.3° upon increasing the external magnetic field. This phase signal intensity of 0.2°–0.3° serves as a reference to distinguish AFM DWs from ferromagnetic-like features exhibiting 10 times larger intensities with similar magnetic tips. Additionally, we note that the shape of the domains remain unaffected by the external field confirming the robust AFM nature of the textures.

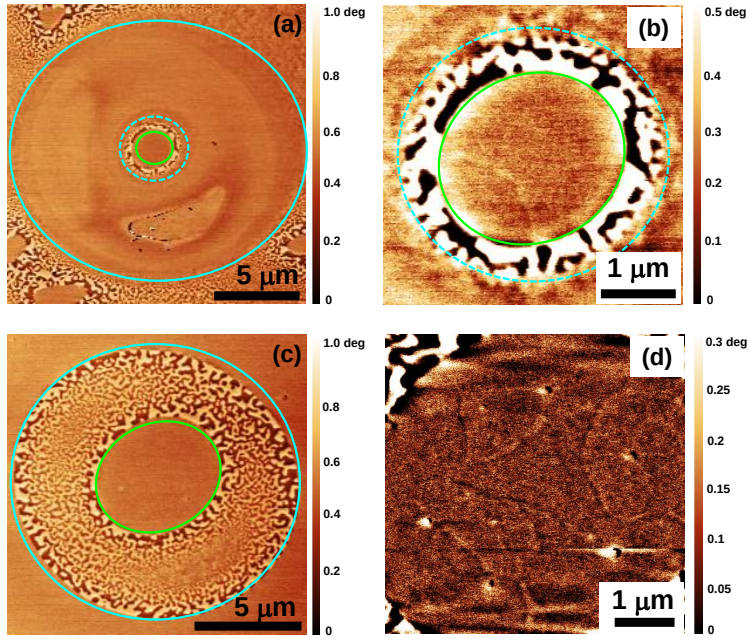

FIGURE 3 Impact of single-shot OAM pulse on the structural and magnetic phase of the SAF: (a), (b) MFM image of the sample after the application of a single shot OAM beam with large energy (~ 810 nJ) for the whole spot and central area with largest OAM, respectively. (c), (d) Similar consequence of single shot OAM beam with lower energy (~ 320 nJ), respectively. The shape of the ring with highest intensity of the OAM beam is contained within the cyan circles/ellipses, whereas the central lowest intensity region is represented by the green circle/ellipse.

In Fig. 3(a)-(d), we illustrate the impact of a single-shot OAM pulse (OAM=+1) on the SAF for two distinct energy levels. The phase scale for each image has been adopted according to the contrast of the texture present in it. The MFM phase image in Fig. 3(a) directly correlates with the topography image presented in Fig. 1(e) for an OAM beam with energy ~ 810 nJ. As anticipated, no phase signal in MFM is observed in the region with the highest energy (ring shape marked by the cyan colored contours), owing to the partial absence of material, which has been completely ablated down to the bottom Pt layer. However, in the higher-resolution image of the central low intensity region (Fig. 3(b)), we can discern a ring (located in-between the cyan and green contours) exhibiting a pronounced magnetic phase change, followed by the center (inside the green contour) featuring the AFM DW (a line-like contrast at the left-bottom region of the green colored contour). The phase associated with the ring exceeds 1.0°, indicating a significant imbalance in the two FM layers within the SAF probably due to excess heating. Nevertheless, the very center of the beam-spot remains apparently undisturbed, displaying the same magnetic DWs as in the pristine state of the SAF. The observation confirms that for extremely high-energy OAM beams, a significant portion of the sample is destroyed, with no noticeable effect at the centre of the beam. In Fig. 3(c) and (d), we present the MFM phase signal corresponding

to a relatively low-energy OAM beam (~ 320 nJ), which is correlated with the topography scans shown in Fig. 1(f). In this case, the peripheral ring-shaped region (with minimal topography changes) exhibits a phase signal of ~ 1.0°, indicating alterations in the properties of the top Co layer. Similar to the previous experiment, the central part of the beam remains unaltered, preserving the pristine SAF state (as seen by the line-like contrasts in (d)). This observation suggests the need to further enhance the influence of OAM at the center of the beam. To address this point, we have assessed the effect of two successive OAM pulses (as opposed to a single-shot approach) with a careful selection of energy.

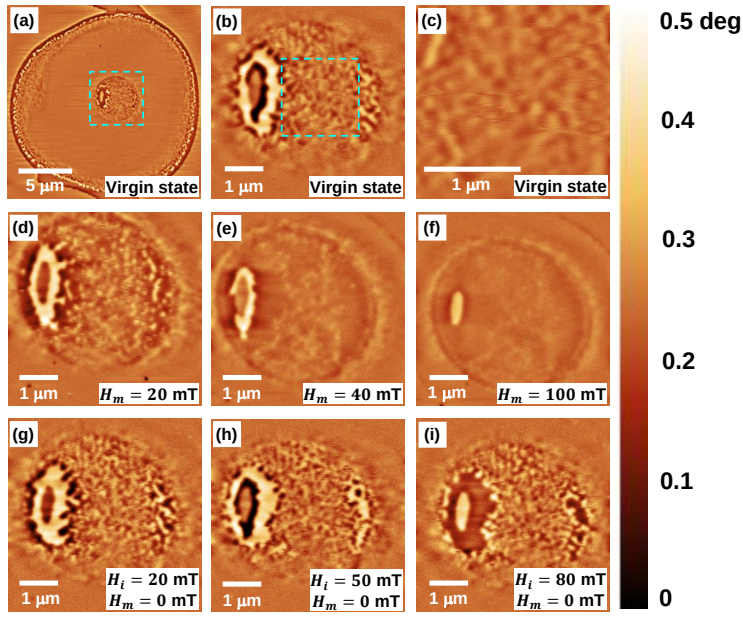

FIGURE 4 MFM study of the sample after double OAM shots: (a) MFM phase of the area with the impact of two-shots OAM pulse with energy ~ 300 nJ. (b) High-resolution phase image of the central area of the OAM shot area as shown by the square shaped box in (a). (c) Zoomed-in phase image of the square box shown in (b). (d)-(f) Field dependent phase images of the same area in (b). (g)-(i) Phase images of the same area measured at remanence after application of various initial magnetic field.

In Fig. 4(a) we show the MFM phase image of the SAF after the impact of two-shot OAM pulses (OAM=+1) with energy ~ 300 nJ for individual pulses and a lag of 1s between them. In order to minimize the thermal energy, the beam energy was chosen a bit lower than that in Fig. 3(c). However, it is worth noting that the application of a two-shot OAM pulse has induced more significant topographic changes compared to the single-shot one. As a result, the film in the high-energy ring-shaped region has been ablated (this can also be observed from the absence of a phase signal in the ring area in (a)). Nonetheless, unlike the experiment in Fig. 3(c), there are observable modifications to the MFM phase at the centre of the laser spot (marked by a cyan color dashed box in Fig. 4(a)), that can be solely attributed to the impact of OAM. For a more in-depth examination, we present a higher-resolution image of the central area in Fig. 4(b). On a small part of the central area towards the left, we observe a more pronounced phase contrast ~0.5°, which can be attributed to minor alterations in the properties of the top Co layer. Nevertheless, in the remainder of the central area, the phase contrast is approximately 0.2°–0.4°, confirming the presence of AFM textures as also evidenced in the

zoomed-in image (Fig. 4(c)) within the square-shaped box marked in (b). The AFM nature of all the textures has been confirmed by measuring the phase signal from the line scan profiles of the images (not shown here). However, it should be noted that although the textures are AFM in nature, they do not represent rigid skyrmions. To gain insight into the nature of these textures, we have investigated the influence of an external field and present the phase images as a function of the varying magnetic field (measurement field: H_m) in Fig. 4(d)-(f). It is evident that within the field range of 100 mT, the AFM textures reach partial saturation, in contrast to the DWs observed in Fig. 2(c)-(e). This observation reinforces the notion that the textures we observe here are stabilized as metastable excitations induced by the transfer of OAM to the SAF. Furthermore, we also have conducted MFM measurements at the remanent state (H_m = 0 mT) after applying various initial external fields (H_i), as depicted in Fig. 4(g)-(i). It is noteworthy that at remanence, the size and density of the skyrmionic textures are maintained, albeit with slight modifications. Consequently, we can conclude that the application of two OAM pulses allows us to transfer finite orbital angular momentum to the SAF, thus nucleating AFM skyrmionic textures. We obtain similar results while measuring an area in the SAF exposed to two OAM pulses of opposite angular momentum (OAM= -1) confirming the robustness of the process (data presented in Fig. S3 in the supplementary information). Therefore, the presence of OAM is important but not its sign. We interpret this result as follows: the OAM transfers some angular momentum to both AF coupled magnetic layers. For an appropriate transfer, it is able to flip the relevant layer for which magnetization opposes the OAM, leaving the other one untouched. At the end of the pulse, the RKKY and DMI interactions stabilise the reversed AF state thus nucleating the skyrmionic entities. However, this approach of two-shots moderate energy OAM beam has two drawbacks: (a) the shape of the nucleated textures is not rigid, and (b) the ring-shaped periphery of the film exposed to the pulse is compromised. Therefore, we shift our approach towards utilizing even lower-energy OAM beams, employing multiple shots rather than just one or two shots, to simultaneously minimize (maximize) the thermal (OAM) contribution.

The impact of multi-shot OAM beams (OAM=+1), with an energy of $\sim$ 84 nJ, a repetition rate of 100 kHz, and an exposure time of 10 ms, on SAF textures under different field histories and remanent states is presented in Fig. 5. The selected energy level ensures that thermal effects are negligible on the sample topography. From a structural perspective, the surface of the SAF exhibits virtually no impact from the OAM beams, as evidenced by a topography signal measuring $\leq$ 1 nm. However, as illustrated in Fig. 5(a), the pulse shape deviates from a near-perfect circle observed in single or double shots, displaying an elliptical distortion (green dashed contour in (a)). This distortion may be attributed to the gradual shift of the laser beam over time during repetition or due to thermal drift. Nevertheless, we have identified a specific region within the beam's shape by considering the phase signal, denoted by a cyan colored square box (Fig. 5(a)), which can be regarded as the cumulative center of the beams. It should be noted that even though multiple pulses have been used, due to significantly lower energy of the individual pulses, we do not observe any ring-shaped destruction of the film along the periphery of the pulses. In Fig. 5(b) and (c), we show the MFM image of the same area as in (a), measured at H_m = 90 mT and at remanence, respectively. We notice a distinctive pattern between (a)-(c) where, within the peripheral region (located between the green elliptical contour and the cyan square box), the film initially saturates and subsequently transitions to a high-contrast (MFM phase $>$ 1.0°) stripe phase. This shift occurs as a result of the imbalance in the SAF, prompted by the influence of laser pulse induced heating. However, the central high phase gradient section of the sample (within the cyan square box) appears relatively unaffected. Higher resolution MFM images at remanence of this central area is depicted in Fig. 5(d) and (e). Here, we observe the formation of robust skyrmionic textures exhibiting a phase akin to what is anticipated in AFM textures. We present the first MFM scan (conducted prior to the application of any external field) of the high OAM region of the sample in Fig. 5(f), revealing isolated skyrmions (depicted as black spots) along with large patches of domains. The skyrmions stabilized in the virgin state have a mean diameter of 66 ± 5 nm with a phase signal of $\sim 0.2 - 0.3°$ (as obtained from the line scans of the textures shown in Fig. 5(p)). This observation distinctly contrasts with the textures

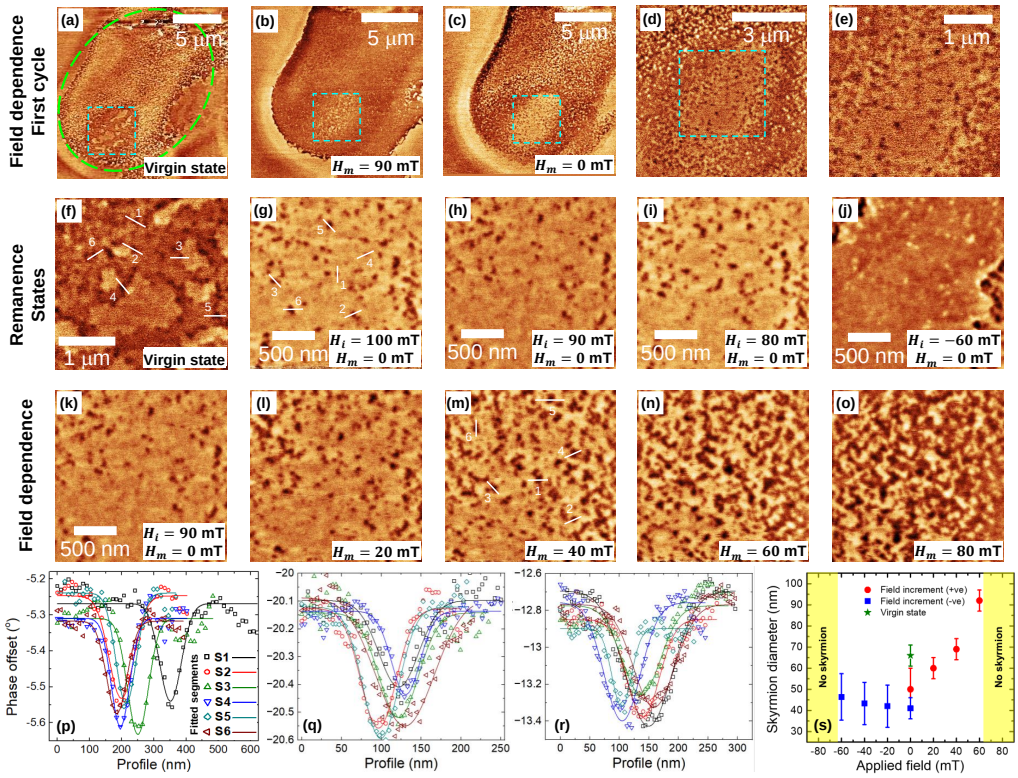

FIGURE 5 **MFM study of the sample after 1000 OAM shots: First row:** field-dependent MFM images of the textures for the first cycle. (a) Phase signal due to the influence of multi-shot OAM on SAF. The green colored dashed contour is a guide to the eye to visualize the elliptical distortion of the laser spot due to multiple shooting. The high OAM area of the total laser spot is represented by a cyan colored square box. (b) MFM image of the same spot as in (a), however performed at an external magnetic field of 90 mT. (c) Same as (b), however measured in the remanent state after removal of the external field. (d) High-resolution image of the square box marked in (c). (e) High-resolution image of the square box marked in (d). **Second row:** (f)-(j) MFM images of the textures of the central high-OAM part of the laser beam measured at remanence after application of various H_i. **Third row:** (k)-(o) evolution of magnetic textures after exposure to several cycles of various H. The scale bar for (k)-(o) are the same and shown in (k). The phase scale bar for all the images is ±0.5°. **Fourth row:** line sections of the phase of MFM scans. (p) Line sections of the MFM signal of the virgin state as marked in (f). (q), (r) Similar line sections of the phase signal as marked in (g) and (m), respectively. The profile of the line sections are fitted with Gaussian curve to find the width (diameter) of the skyrmions. (s) Diameter of skyrmions as a function of polarity and amplitude of external magnetic field.

produced by single or double-shot OAM pulses. Further, during the field dependence of such textures we observe a continuous evolution of the large domains, whereas the dark textures remain intact albeit with some modifications in size. To gain deeper insights into the property of these textures, we performed MFM measurements in the remanent state within the same area, prior to subjecting the sample to various initial magnetic fields (H_i) as illustrated in Fig. 5(g)-(j). It is worth noting that the prominent large patches observed in the virgin state are absent in the SAF after the initial saturation (Fig. 5(e)). In Fig. 5(g), only the black skyrmionic textures persist as metastable excitations against a uniform background. In Fig. 5(g)-(i), we depict these same skyrmionic states at remanence with initial magnetic field

strengths of H_i = 100, 90, and 80 mT, respectively. In each case, we obtain skyrmions of similar size (50 ± 10 nm) within the error bar (line scans in Fig. 5(q)). This reveals that the skyrmions stabilized through field history at remanence are more compact than the ones stabilized in the virgin state prior to application of an external field. This observation aligns with findings previously reported for FM skyrmions obtained in zero magnetic field [22]. Furthermore, we note that if we reverse the initial magnetic field ($H_i = -60$ mT) in the opposite direction, the phase of the textures changes from attractive to repulsive while exhibiting consistent behavior (Fig. 5(j)). As discussed by Legrand et al. [16], the apparent skyrmion diameter in MFM measurements is often overestimated by 30-50% compared to the actual value due to the interaction of skyrmions with the moment of the magnetic tip. Hence, we conclude that using this method, we have stabilized compact DMI skyrmions with diameter < 50 nm. It is noteworthy that the metastable skyrmionic textures nucleated at remanence demonstrate a remarkable stability over extended periods, lasting for weeks, and are primarily modified by varying the initial magnetic field strength, H_i.

A compelling piece of evidence confirming the imprinted AFM texture in the SAF is the noticeable change in the size of the skyrmions in response to an external magnetic field (H_m). To investigate this phenomenon further, we have conducted additional field-dependent measurements on the textures, as depicted in Fig. 5(k)-(o). Here, the rigid skyrmionic textures exhibit an increase in size at the expense of the previously bright, uniform background. We see that the mean skyrmion diameter and intensity of the phase signal are 60 ± 5 nm, 0.4°; 69 ± 5 nm, 0.7°; and 92 ± 5 nm, 0.8°, for H_m = 20 mT (Fig.5(l)); H_m = 40 mT (Fig.5(m)); and H_m = 60 mT (Fig.5(n)), respectively. A comparison of skyrmion sizes as a function of the polarity and magnitude of the external field is presented in Fig. 5(s). As discussed before, the skyrmion imprinted in the virgin state (immediately after exposure to the OAM beam and before any field history) is larger than those stabilized at remanence following the application of a negative or positive external field. This behavior is predominantly attributed to the reorientation of the spins and the confinement effect of the external field. Interestingly, the skyrmion size increases with the magnetic field for positive polarity, whereas it remains invariant for negative polarity. The variation of skyrmion size with the polarity and strength of the external field is mainly driven by the tip-sample interaction. Even at zero external field (ignoring the tip magnetization), the different distances of the layers from the magnetic tip contribute to a finite MFM phase signal. The stray field arises from both magnetic layers, with the top layer (closer to the tip) contributing more than the bottom one. When the external field remains below the SAF effective field (as in the present case), only the magnetization of the tip aligns with the external field. Skyrmions then slightly shrink or expand in both layers depending on the external field. Considering two separate cases where the external field (H_{ext}) is negative ($H_{ext} < 0$) or positive ($H_{ext} > 0$), we assume that the top layer background is saturated *down* (down spin pointing towards $H_{ext} < 0$) with a skyrmion core pointing *up*, and the bottom layer background is saturated *up* with a skyrmion core pointing *down* (see supplementary Fig. S4 for detailed micromagnetic representation). This discussion also applies to the opposite orientation. Under these circumstances, when $H_{ext} < 0$, the signal from the top layer skyrmion decreases, whereas the signal from the bottom layer skyrmion increases. However, the bottom layer generally contributes less due to the larger distance from the magnetic tip. As the skyrmion core in the bottom layer increases, the signal becomes stronger. This competition between the two counteracting effects initially leads to a shrinkage in skyrmion size (top layer) followed by field-invariant behavior. Beyond a certain threshold external field, the bottom layer dominates, and rigid skyrmions become unstable. In the scenario where $H_{ext} > 0$, the tip magnetization points *up*. Here, the signal from the top layer skyrmion core increases, while that from the bottom layer decreases. Since the top layer contributes more to the phase signal in MFM, the skyrmion size increases with the increasing external field. Additionally, when the MFM signal is normalized (and we perform FWHM), we obtain even larger values because the background is non-zero, opposite to the value of the core. However, it is crucial to emphasize that, when the external field is removed, the skyrmionic textures recover their compact shape. This underscores the enduring stability of the textures, reaffirming the profound influence of the underlying AFM

coupling and implication of the OAM beam. To distinguish between the influence of temperature and of OAM in nucleating skyrmionic textures, we conducted parallel experiments using exposition to multiple Gaussian pulses with comparable specifications. Our observations indicate that while AFM spin textures are stabilized in the Gaussian beam under appropriate energy conditions, skyrmionic textures are absent both at remanence and throughout the magnetic field history. A comprehensive analysis of the impact of Gaussian beam on spin textures is discussed in Fig. S2 in supplementary information. Finally, the intensity of the laser spot in the vortex beam (Fig. 1(d)) is similar at the centre and just outside the periphery, with a notable difference in the spatial gradient of the phase. However, we obtain no alteration in the MFM phase outside the elliptical beam spot irrespective of the field history. The aforementioned discussion concludes that the AFM skyrmionic spin textures stabilized in our system is a combined effect of the thermal energy and of the OAM of the laser beams.

4 | CONCLUSION

In summary, we demonstrate a proof-of-concept showcasing the stabilization of compact DMI skyrmions (diameter < 50 nm) within non-biased SAFs using OAM vortex laser beams, all in the absence of an external magnetic field. Our findings confirm that both temperature and the magneto-electric coupling induced by the OAM beam are critical in imprinting these skyrmionic textures onto the SAF. However, to efficiently manipulate the shape, size, and distribution of these skyrmionic textures while maintaining a well-balanced SAF, it is essential to minimize the effects of thermal energy and simultaneously enhance the influence of the OAM beam. Our results underscore the importance of fine-tuning beam energy, exposure time, and the number of pulses to achieve the desired state. Interestingly, this interaction and momentum transfer from light to the material occur on a femtosecond timescale in a single shot, whereas multiple low-energy shots result in more sustainable skyrmion writing. A potential future direction would be to use longer mid-infrared wavelengths to further minimize thermal effects. This work is anticipated to open a new research paradigm for the use of optical vortex beams in generating antiferromagnetic textures, addressing the limitations of electrical manipulation due to sample-specific design complexities.

Acknowledgements

The authors acknowledge Nicolas Reyren and Jean-Yves Chauleau for fruitful discussions and comments on the manuscript. Financial support from the European Union's Horizon 2020 research and innovation programme under the Grant No. 964931 (TSAR), from the CEFIPRA project and from a government grant managed by the ANR as part of the France 2030 investment plan from PEPR SPIN ANR-22-EXSP 0002 (CHIREX) are acknowledged.

Conflict of interest

There is no conflict of interest.

Supporting Information

A supplementary text file is available online for the paper.

references

[1] Fert A, Reyren N, Cros V. Magnetic skyrmions: advances in physics and potential applications. Nature Review Materials 2017;2(7):17031. https://doi.org/10.1038/natrevmats.2017.31.

[2] Jiang W, Zhang X, Yu G, Zhang W, Wang X, Jungfleisch MB, et al. Direct observation of the skyrmion Hall effect. Nature Physics 2017;13(2):162–169. https://doi.org/10.1038/nphys3883.

[3] Litzius K, Lemesh I, Krüger B, Bassirian P, Caretta L, Richter K, et al. Skyrmion Hall effect revealed by direct time-resolved X-ray microscopy. Nature Physics 2017;13(2):170–175. https://doi.org/10.1038/nphys4000.

[4] Fert A, Cros V, Sampaio J. Skyrmions on the track. Nature Nanotechnology 2013;8(3):152–156. https://doi.org/10.1038/nnano.2013.29.

[5] Liu Y, Lei N, Wang C, Zhang X, Kang W, Zhu D, et al. Voltage-Driven High-Speed Skyrmion Motion in a Skyrmion-Shift Device. Phys Rev Appl 2019 Jan;11:014004. https://link.aps.org/doi/10.1103/PhysRevApplied.11.014004.

[6] Bernand-Mantel A, Fondet A, Barnova S, Simon TM, Muratov CB. Theory of magnetic field stabilized compact skyrmions in thin-film ferromagnets. Phys Rev B 2023 Oct;108:L161405. https://link.aps.org/doi/10.1103/PhysRevB.108.L161405.

[7] Woo S, Litzius K, Krüger B, Im MY, Caretta L, Richter K, et al. Observation of room-temperature magnetic skyrmions and their current-driven dynamics in ultrathin metallic ferromagnets. Nature Materials 2016;15(5):501–506. https://doi.org/10.1038/nmat4593.

[8] Ojha B, Mallick S, Panigrahy S, Sharma M, Thiaville A, Rohart S, et al. Driving skyrmions with low threshold current density in Pt/CoFeB thin film. Physica Scripta 2023 Feb;98:035819. https://dx.doi.org/10.1088/1402-4896/acb862.

[9] Barker J, Tretiakov OA. Static and Dynamical Properties of Antiferromagnetic Skyrmions in the Presence of Applied Current and Temperature. Phys Rev Lett 2016 Apr;116:147203. https://link.aps.org/doi/10.1103/PhysRevLett.116.147203.

[10] Zhang X, Zhou Y, Ezawa M. Antiferromagnetic Skyrmion: Stability, Creation and Manipulation. Scientific Reports 2016 Apr;6:24795. https://doi.org/10.1038/srep24795.

[11] Mallick S, Sassi Y, Prestes NF, Krishnia S, Gallego F, Denneulin T, et al. Driving skyrmions in flow regime in synthetic ferrimagnets. arXiv 2023;2305.19208v2.

[12] Pham VT, Sisodia N, Di Manici I, Urrestarazu-Larrañaga J, Bairagi K, Pelloux-Prayer J, et al. Fast current-induced skyrmion motion in synthetic antiferromagnets. Science 2024 April;384:307–312. https://doi.org/10.1126/science.add5751.

[13] Panigrahy S, Mallick S, Sampaio Ja, Rohart S. Skyrmion inertia in synthetic antiferromagnets. Phys Rev B 2022 Oct;106:144405. https://link.aps.org/doi/10.1103/PhysRevB.106.144405.

[14] Zhang X, Zhou Y, Ezawa M. Magnetic bilayer-skyrmions without skyrmion Hall effect. Nature Communications 2016;7(1):10293. https://doi.org/10.1038/ncomms10293.

[15] Duine RA, Lee KJ, Parkin SSP, Stiles MD. Synthetic antiferromagnetic spintronics. Nature Physics 2018;14(3):217–219. https://doi.org/10.1038/s41567-018-0050-y.

[16] Legrand W, Maccariello D, Ajejas F, Collin S, Vecchiola A, Bouzehouane K, et al. Room-temperature stabilization of antiferromagnetic skyrmions in synthetic antiferromagnets. Nature Materials 2020;19(1):34–42. https://doi.org/10.1038/s41563-019-0468-3.

[17] Parkin SSP. Systematic variation of the strength and oscillation period of indirect magnetic exchange coupling through the 3d, 4d, and 5d transition metals. Phys Rev Lett 1991 Dec;67:3598–3601. https://link.aps.org/doi/10.1103/PhysRevLett.67.3598.

[18] Bhukta M, Singh BB, Mallick S, Rohart S, Bedanta S. Degenerate skyrmionic states in synthetic antiferromagnets. Nanotechnology 2022 jun;33(38):385702. https://dx.doi.org/10.1088/1361-6528/ac7471.

[19] Rana KG, Finco A, Fabre F, Chouaieb S, Haykal A, Buda-Prejbeanu LD, et al. Room-Temperature Skyrmions at Zero Field in Exchange-Biased Ultrathin Films. Phys Rev Appl 2020 Apr;13:044079. https://link.aps.org/doi/10.1103/PhysRevApplied.13.044079.

[20] Behera AK, Mishra SS, Mallick S, Singh BB, Bedanta S. Size and shape of skyrmions for variable Dzyaloshinskii–Moriya interaction and uniaxial anisotropy. Journal of Physics D: Applied Physics 2018 jun;51(28):285001. https://dx.doi.org/10.1088/1361-6463/aac9a7.

[21] Ho P, Tan AKC, Goolaup S, Oyarce ALG, Raju M, Huang LS, et al. Geometrically Tailored Skyrmions at Zero Magnetic Field in Multilayered Nanostructures. Phys Rev Appl 2019 Feb;11:024064. https://link.aps.org/doi/10.1103/PhysRevApplied.11.024064.

[22] Mallick S, Panigrahy S, Pradhan G, Rohart S. Current-Induced Nucleation and Motion of Skyrmions in Zero Magnetic Field. Phys Rev Appl 2022 Dec;18:064072. https://link.aps.org/doi/10.1103/PhysRevApplied.18.064072.

[23] Duong NK, Raju M, Petrović AP, Tomasello R, Finocchio G, Panagopoulos C. Stabilizing zero-field skyrmions in Ir/Fe/Co/Pt thin film multilayers by magnetic history control. Applied Physics Letters 2019 02;114(7):072401. https://doi.org/10.1063/1.5080713.

[24] Masell J, Rodrigues DR, McKeever BF, Everschor-Sitte K. Spin-transfer torque driven motion, deformation, and instabilities of magnetic skyrmions at high currents. Phys Rev B 2020 Jun;101:214428. https://link.aps.org/doi/10.1103/PhysRevB.101.214428.

[25] Juge R, Sisodia N, Larrañaga JU, Zhang Q, Pham VT, Rana KG, et al. Skyrmions in synthetic antiferromagnets and their nucleation via electrical current and ultra-fast laser illumination. Nature Communications 2022 August;13:4807. https://doi.org/10.1038/s41467-022-32525-4.

[26] Fujita H, Sato M. Ultrafast generation of skyrmionic defects with vortex beams: Printing laser profiles on magnets. Phys Rev B 2017 Feb;95:054421. https://link.aps.org/doi/10.1103/PhysRevB.95.054421.

[27] Fujita H, Sato M. Encoding orbital angular momentum of light in magnets. Phys Rev B 2017 Aug;96:060407. https://link.aps.org/doi/10.1103/PhysRevB.96.060407.

[28] Edström A, Lubk A, Rusz J. Elastic Scattering of Electron Vortex Beams in Magnetic Matter. Phys Rev Lett 2016 Mar;116:127203. https://link.aps.org/doi/10.1103/PhysRevLett.116.127203.

[29] Mahdavi M, Sabegh ZA, Hamedi HR, Mahmoudi M. Orbital angular momentum transfer in molecular magnets. Phys Rev B 2021 Sep;104:094432. https://link.aps.org/doi/10.1103/PhysRevB.104.094432.